Applied Physics Letters

Non-resonant metasurface for broadband elastic wave mode splitting

Cite as: Appl. Phys. Lett. **116**, 171903 (2020); https://doi.org/10.1063/5.0005408
Submitted: 20 February 2020 . Accepted: 09 April 2020 . Published Online: 27 April 2020

Mingye Zheng, Chung Il Park, Xiaoning Liu, Rui Zhu, Gengkai Hu, and Yoon Young Kim

Non-resonant metasurface for broadband elastic wave mode splitting

Cite as: Appl. Phys. Lett. **116**, 171903 (2020); doi: 10.1063/5.0005408
Submitted: 20 February 2020 · Accepted: 9 April 2020 ·
Published Online: 27 April 2020

View Online Export Citation CrossMark

Mingye Zheng,[1,2] Chung Il Park,[2] Xiaoning Liu,[1] Rui Zhu,[1,a)] Gengkai Hu,[1,a)] and Yoon Young Kim[2,a)]

AFFILIATIONS

[1]Key Laboratory of Dynamics and Control of Flight Vehicle, Ministry of Education, School of Aerospace Engineering, Beijing Institute of Technology, Beijing 100081, China
[2]School of Mechanical and Aerospace Engineering, and Institute of Advanced Machines and Design, Seoul National University, 1 Gwanak-ro, Gwanak-gu, Seoul 08826, South Korea

[a)]Authors to whom correspondence should be addressed: ruizhu@bit.edu.cn, hugeng@bit.edu.cn and yykim@snu.ac.kr

ABSTRACT

Complex polarizations of elastic waves allow mode conversions between two solids, making wave mode separation extremely difficult even for a narrow frequency range with resonant metamaterials. In this Letter, a non-resonant elastic metasurface design is proposed to achieve a perfect splitting of longitudinal and shear waves in space. The key to this broadband design is a singly polarized solid with engineered static elastic tensor, which provides a tool to tune the polarization through non-resonant microstructure design. Both full-wave simulations and experiments are conducted to validate the mode splitting function of the designed metasurface. Potential applications such as elastic wave shifting and selective wave mode focusing are also demonstrated. This research provides an alternative route to design broadband and compact metasurfaces for elastic wave communications, biomedical diagnosis, and wave-based damage evaluations.

In recent years, a rapid growth of research in acoustic and electromagnetic (EM) wave manipulation via metamaterials has been observed.[1–3] Compared to bulky metamaterials, the metasurface is a planar version of metamaterials with compact microstructures for purposed wave engineering. It is first conceived for EM waves to tune the refraction[4] and extended straightforwardly to acoustic wave manipulations.[5–9]

Unlike in acoustic or EM waves, the wave manipulation of elastic waves[10–14] is facing severe difficulties that are closely related to the more complex wave polarization characteristics in solids than that in air or fluid. The emergence of resonance-based elastic metamaterials (EMMs) provides a very efficient way to achieve peculiar wave trajectory manipulations[15–18] and elastic wave mode separation/conversion[19–23] in a certain frequency range. Various resonance-based elastic metasurface designs have also been explored.[24–28] Lee *et al.*[24] designed a metasurface that can achieve full transmission beam steering of longitudinal (L) waves by independently amplifying the effective mass and weakening stiffness. Kim *et al.*[25] also used the metasurface to realize the broad-angle mode conversion of elastic waves. More recently, Cao *et al.*[26] introduced the concept of disorder effects into the elastic metasurface and realized anomalous deflection and focusing effects of flexural waves, which expanded the category of elastic metasurfaces. However, the undesired narrow band and loss intrinsically associated with the resonant microstructures severely restrict the practical applications of elastic metasurfaces. To overcome the limitations of resonance, Zheng *et al.*[29] designed a non-resonance singly polarized solid (SPS), which can be a good starting point for broadband elastic metasurface design.

In this Letter, a non-resonant elastic metasurface will be proposed and validated, which can completely split L and shear (S) waves in space with desired propagating directions and minimum losses over a broad frequency range. Peculiar elastic wave controls, such as elastic wave shifting and selective wave mode focusing, will also be demonstrated, providing an alternative route for elastic wave communication or biomedical imaging applications.

Two wave modes, namely L and S waves orthogonal each other, are supported in two-dimensional (2D) isotropic solids (C_{11}, C_{66}, ρ). Conversions between these two wave modes occur when oblique incidences happen at the interface between two different media. This results in extremely complex reflection and transmission responses even for a sandwiched solid layer case, as shown in Fig. 1(a). With an SPS[29] being replaced in the sandwiched layer, we can simplify the wave responses, as shown in Fig. 1(b). The SPSs through microstructure design allow only one transmitted mode and therefore reduce the number of the reflected and transmitted waves. Further investigation shows that the positive SPS ($C_{11}^S = C_{22}^S, C_{12}^S > 0, \rho_s$) supports only limited polarization and is unable to fulfill the wave mode splitting (see the supplementary material). Thus, a negative SPS ($C_{11}^S = C_{22}^S, C_{12}^S < 0, \rho_s$, the same as below) is selected to design the elastic metasurface, which completely splits the L and S waves in space, as shown schematically in Fig. 1(c).

The key to the wave mode splitting is the negative SPS's unique wave property. Figure 1(d) shows the equi-frequency curve (EFC) and the supported wave polarization vectors in a negative SPS. Comparing with conventional solids, it can be found that the negative SPS has only one circular EFC with all possible polarization angles (from 0° to 90°). In addition, by rotating the angle ϕ between the global coordinate system and the SPS's principal axis, supported wave polarization can be adjusted accordingly, which is very convenient for subsequent metasurface design.

Following the analysis inside the SPS, the wave behavior at the two interfaces between the SPS and the isotropic matrix solids is then studied. First, the upper interface under S-wave incidence is considered with the EFCs of the two media being shown in Fig. 2(a). Based on the Snell law, it can be found that the reflected L wave and transmitted wave vanish for $\theta^i > \theta^{cr1} = \sin^{-1}(k_L/k_S)$ and $\theta^i > \theta^{cr2} = \sin^{-1}(k_T/k_S)$, respectively. Here, θ^i denotes the incident angle and k_L, k_S denote the wave vectors of L and S waves, respectively. As a result, a total reflection of the S wave can be obtained when

$$\theta^i > \theta^{cr} = \max\left(\theta^{cr1}, \theta^{cr2}\right). \quad (1)$$

In order to achieve the perfect wave mode splitting result in Fig. 1(c), a total transmission of an L wave should also be satisfied. For an

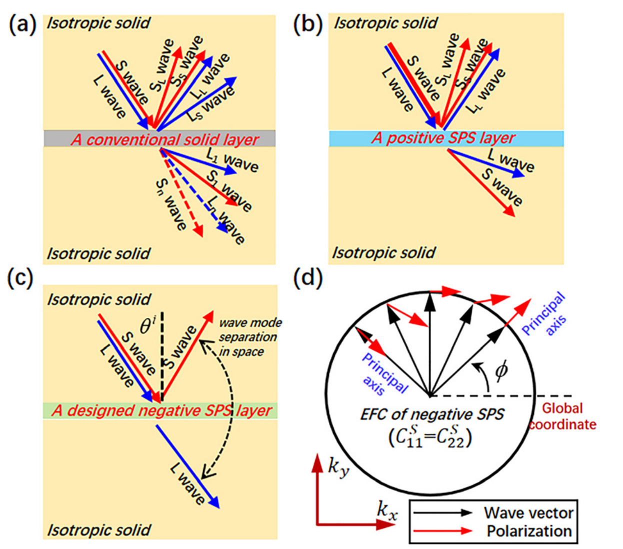

FIG. 1. The wave responses in (a) a conventional solid, (b) a positive SPS, and (c) a negative SPS that is sandwiched into isotropic solids under simultaneous L and S wave incidences. (d) The equi-frequency curve (EFC) of a negative SPS with the wave polarization vectors.

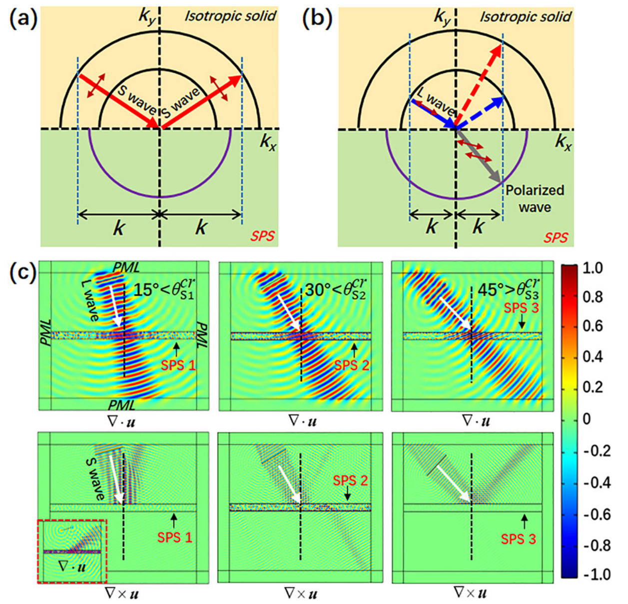

FIG. 2. The EFC analysis based on SPS and isotropic solid under (a) S-wave (total reflection) and (b) L-wave incidences, respectively. (c) The simulation results based on SPSs under the L-and S-wave incidences at 15°, 30°, and 45°.

oblique L-wave incidence in Fig. 2(b), the total transmission of an L wave means that both reflected L and S waves should be eliminated, which implies a generalized L-wave impedance matching condition (a detailed derivation can be found in the supplementary material)

$$Z_T^S = Z_L + Z^*, \quad (2a)$$

where $Z_T^S = \sqrt{C_{11}^S \rho_s}/\cos\theta^t$ represents the generalized impedance of the transmitted wave in the SPS (θ^t denotes the transmitted angle) and $Z_L = \sqrt{C_{11}\rho}/\cos\theta^i$ represents the generalized impedance of an L wave in the isotropic solid. Besides, an additional impedance term, $Z^* = \frac{4\sqrt{\rho}C_{66}^2 \sin^2\theta^i}{C_{11}\sqrt{C_{11}}\cos\theta^i} - \frac{4\sqrt{\rho}C_{66}\sin^2\theta^i}{\sqrt{C_{11}}\cos\theta^i}$, needs to be added in the matching condition to compensate the shear effect in solids. It should also be mentioned that the principal orientation of SPS ϕ also needs to satisfy the following condition:

$$\tan 2\phi = \frac{C_{66}\sin 2\theta^i}{\left(C_{11} - C_{66} + C_{66}\cos 2\theta^i\right)}. \quad (2b)$$

Numerical simulations with three incident angles $\theta^i = 15°, 30°$, and 45° were conducted to validate the derived wave mode splitting conditions. Based on Eqs. (2a) and (2b), three metasurfaces were designed for the corresponding incident angles. θ_{S1}^{cr}, θ_{S2}^{cr}, and θ_{S3}^{cr} are the derived critical angles for the total S-wave reflections in the three cases, respectively. The corresponding normalized L- and S- wave field results of the three cases are shown in Fig. 2(c). First, it can be found from the three L-wave fields that total L-wave transmissions are achieved for all three cases. Second, only the third case shows the total S-wave reflection since only $\theta^i = 45°$ is larger than its corresponding critical angle θ_{S3}^{cr} as predicated by Eq. (1). Therefore, the simulation results verify the above derivations.

Based on the above analysis, a concave hexagon configuration was first chosen as the candidate microstructure of the SPS, and the trapezoidal masses were added to meet the required impedance matching conditions,[30,31] as shown in Fig. 3(a). Then, numerical simulations were performed with the incident angle being $\theta^i = 45°$. By using the numerical-based effective medium method,[29,30] the corresponding effective material parameters and geometric parameters of the aluminum-based SPS unit cell can be found in the supplementary material. As shown in the normalized simulation results in Fig. 3(a), with the L-wave incidence into the SPS metasurface at 45°, the transmitted L wave still propagates along its original direction, while no reflected L wave is observed. On the contrary, the incident S wave is totally reflected by the metasurface. As a result, the designed elastic metasurface is shown to completely split the incident L and S waves and guide them along the two orthogonal directions. Note that in our simulations, the very tiny principal orientation $\phi = 3.131°$ calculated from Eq. (2b) can be approximated by $\phi = 0$, which in fact can make the boundary of the metasurface simpler and the overall pattern easier for fabrication. (Details can be seen in the supplementary material.)

Furthermore, Figs. 3(b) and 3(c) confirm the broadband feature of the designed elastic metasurface in wave mode splitting. To obtain the results in Figs. 3(b) and 3(c), both COMSOL simulations and transient experiments were conducted from 50 to 80 kHz with an increment of 10 kHz. (The related details can be seen in the supplementary material.) When the L wave is incident, it is found that the transmitted energy rates obtained from both experiments and simulations are mostly above 90%, while the reflected energy rates are mostly less than 10%, as shown in Fig. 3(b). When the S wave is incident, on the contrary, the reflected energy rates reach almost 100% with the transmitted energy rates being close to zero, as shown in Fig. 3(c). Therefore, the broadband feature is well verified both by the numerical and experimental results, which also agree well with each other.

For experiments, the elastic metasurface having the designed microstructure pattern was fabricated in an aluminum plate by a laser cutting technique, as shown in Fig. 4(a). As indicated in the supplementary material, the performance of the designed SPS is not sensitive to possible machining errors. To bridge the impedance mismatch between the aluminum background and the elastic metasurface, four columns of circular holes with a specific radius were machined to match the L-wave impedance of the metasurface. Then, eight columns of circular holes with the gradually changing radius are machined as a transition medium, as shown in Fig. 4(a). (See details in the supplementary material.) A transmitter (piezoelectric lead zirconate titanate (PZT) in a d31 mode for the L wave and a magnetostrictive patch transducer (MPT) for the S wave) is put on one side of the intermediate structure to excite the L or S wave, and two sensors [electromagnetic acoustic transducers (EMATs) for the L wave and periodical permanent magnet electromagnetic acoustic transducers (PPM-EMATs) for the S wave][24,32] are symmetrically located on both sides of the metasurface to measure the transmitted signal (Sensor 1)

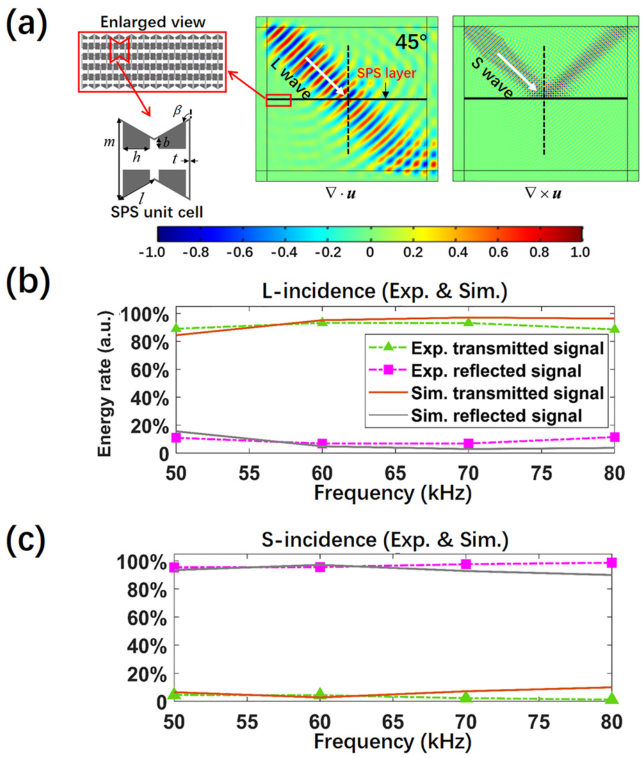

FIG. 3. (a) The detailed microstructure of the designed metasurface and the simulation results under the L-wave or S-wave incidence. The energy rates of transmission and reflection at different frequencies under (b) the L-wave incidence and (c) the S-wave incidence.

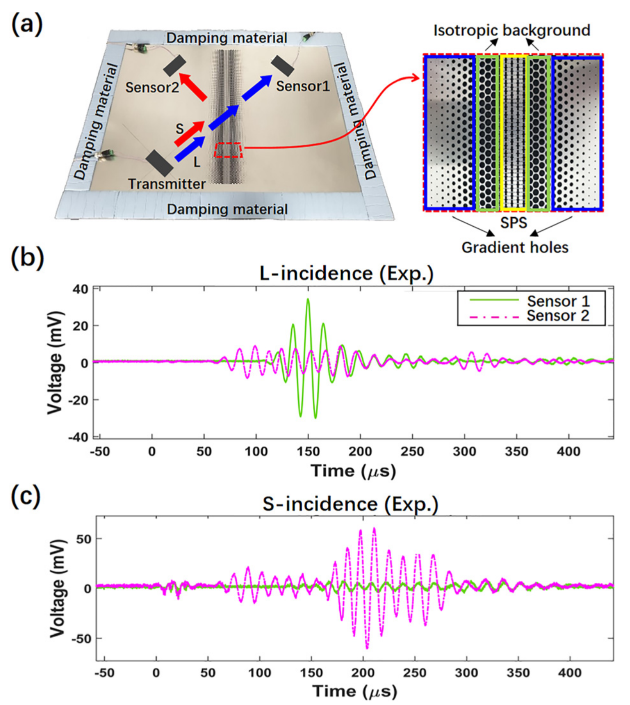

FIG. 4. (a) Experimental system and the enlarged view of machined microstructures. The experimental time-domain signals measured by Sensor 1 and Sensor 2 under the L wave's incidence (b) and S wave's incidence (c) at 70 kHz, respectively. In (b) and (c), the green solid and magenta dashed lines represent the transmitted and reflected signals, respectively.

and reflected signal (Sensor 2), respectively. Blu-tack, a strong dissipation material, was attached along the edges of the aluminum plate to ensure a good absorption of boundary-reflected waves,[33] as shown in Fig. 4(a). Other details of the experimental setup can be seen in the supplementary material.

The experimentally measured time-domain signals for the L- and S-wave incidences at 70 kHz are also shown in Figs. 4(b) and 4(c), respectively. It can be found that the amplitudes of the transmitted signals are 3–4 times larger than those of the reflected signals, which means that the L wave can nearly pass through the metasurface, as shown in Fig. 4(b). On the contrary, almost all S waves are totally reflected, as shown in Fig. 4(c). For better comparison, the same wave experiments were performed with a reference aluminum plate that has only the effective isotropic background and perforated aluminum with gradient holes. (See Fig. S9 in the supplementary material.) The results show that both the L and S waves are transmitted with little reflection for the case of the reference aluminum plate. Therefore, it is concluded that the proposed elastic metasurface in a wide range of frequencies can achieve the 2D elastic wave mode splitting in space.

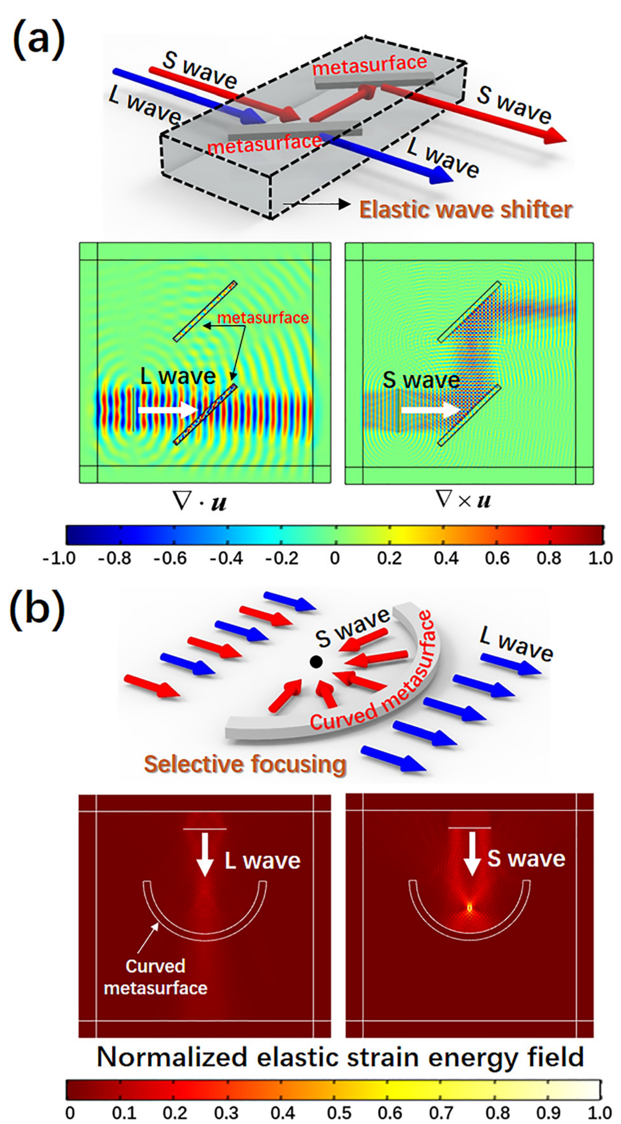

FIG. 5. Application examples with simulation results for (a) shifting of the S-wave mode only and (b) selective focusing of the S-wave mode.

Last but not least, two potential applications of the achieved elastic metasurface for wave mode splitting are explored. As the first example, an elastic wave shifter can be designed, as shown in Fig. 5(a). Like a periscope, the S wave can be shifted by a certain distance and continue to travel parallel to the L wave. As the second example, a curved elastic metasurface, as shown in Fig. 5(b), can achieve selected wave mode focusing. The L waves can pass with little reflection, while the S waves are reflected and focused at the focal point. These applications can be potentially useful in elaborately manipulating specific wave modes.

In summary, a compact and non-resonant elastic metasurface, with approximately 1/5 of the L-wave's wavelength, was designed and fabricated for broadband selective wave mode control. Based on the generalized L-wave impedance matching condition and the Snell law, the designed elastic metasurface is shown to be able to completely separate L and S waves and guide them to propagate along two separated directions, which are validated by both numerical simulations and experiments. As potential applications of the metasurface, the shifting and focusing of the S-wave mode among compound L and S waves were also demonstrated. The proposed SPS metasurface is broadband in nature and is more advantageous compared with common resonance-based metasurfaces in the fields of elastic wave devices and communications.

See the supplementary material for details.

This work was supported by the Global Frontier Project on Center for Advanced Meta-Materials (CAMM) funded by the National Research Foundation (NRF) under the Ministry of Science, ICT and Future Planning, Korea (No. CAMM-2014M3A6B3063711), through the Institute of Advanced Machines and Design (IAMD). The support from the National Science Foundation of China (NSFC) (Nos. 11632003, 11872112, 11991030, 11991033, and 111 Project B16003) is greatly appreciated. Mingye Zheng also acknowledges the financial support from the China Scholarship Council.

The data that support the findings of this study are available within the article and its supplementary material.

REFERENCES

[1]S. A. Cummer, J. Christensen, and A. Alù, Nat. Rev. Mater. **1**, 16001 (2016).
[2]R. A. Shelby, D. R. Smith, and S. Schultz, Science **292**, 77 (2001).
[3]D. Schurig, J. J. Mock, B. J. Justice, S. A. Cummer, J. B. Pendry, A. F. Starr, and D. R. Smith, Science **314**, 977 (2006).
[4]N. Yu, P. Genevet, M. A. Kats, F. Aieta, J. P. Tetienne, F. Capasso, and Z. Gaburro, Science **334**, 333 (2011).
[5]Y. Li, X. Jiang, B. Liang, J. Cheng, and L. Zhang, Phys. Rev. Appl. **4**, 024003 (2015).
[6]X. Jiang, Y. Li, B. Liang, J. Cheng, and L. Zhang, Phys. Rev. Lett. **117**, 034301 (2016).
[7]Y. Li, C. Shen, Y. Xie, J. Li, W. Wang, S. A. Cummer, and Y. Jing, Phys. Rev. Lett. **119**, 035501 (2017).
[8]X. Wang, D. Mao, and Y. Li, Sci. Rep. **7**, 11604 (2017).

[9]B. Assouar, B. Liang, Y. Wu, Y. Li, J. Cheng, and Y. Jing, Nat. Rev. Mater. **3**, 460 (2018).
[10]J. L. Rose, *Ultrasonic Guided Waves in Solid Media* (Cambridge University Press, 2014).
[11]D. N. Alleyne and P. Cawley, IEEE Trans. Ultrason., Ferroelectr., Freq. Control **39**, 381 (1992).
[12]B. F. Kennedy, P. Wijesinghe, and D. D. Sampson, Nat. Photonics **11**, 215 (2017).
[13]Y. Jin, Y. Ying, and D. Zhao, Proc. Meet. Acoust. **20**, 45001 (2013).
[14]S. Gong and G. Piazza, "Overmoded shear horizontal wave MEMS resonators using X-cut lithium niobate thin film," in *2014 IEEE International Ultrasonics Symposium* (IEEE, 2014), pp. 568–571.
[15]R. Zhu, X. N. Liu, G. K. Hu, C. T. Sun, and G. L. Huang, Nat. Commun. **5**, 5510 (2014).
[16]X. Yan, R. Zhu, G. Huang, and F. Yuan, Appl. Phys. Lett. **103**, 121901 (2013).
[17]A. Liu, X. Zhou, G. Huang, and G. Hu, J. Acoust. Soc. Am. **132**, 2800 (2012).
[18]M. Farhat, S. Guenneau, and S. Enoch, Phys. Rev. Lett. **103**, 024301 (2009).
[19]X. Su, Z. Lu, and A. N. Norris, J. Appl. Phys. **123**, 091701 (2018).
[20]J. M. Kweun, H. J. Lee, J. H. Oh, H. M. Seung, and Y. Y. Kim, Phys. Rev. Lett. **118**, 205901 (2017).
[21]X. Yang and Y. Y. Kim, Compos. Struct. **201**, 161 (2018).
[22]X. Yang, J. M. Kweun, and Y. Y. Kim, Sci. Rep. **8**, 69 (2018).
[23]M. K. Lee, P. S. Ma, I. K. Lee, H. W. Kim, and Y. Y. Kim, Appl. Phys. Lett. **98**, 011909 (2011).
[24]H. Lee, J. K. Lee, H. M. Seung, and Y. Y. Kim, J. Mech. Phys. Solids **112**, 577 (2018).
[25]M. Kim, W. Lee, Y. Y. Kim, and J. Oh, Appl. Phys. Lett. **112**, 241905 (2018).
[26]L. Cao, Z. Yang, Y. Xu, S. Fan, Y. Zhu, Z. Chen, B. Vincent, and B. Assouar, Phys. Rev. Appl. **13**, 014054 (2020).
[27]X. Guo, V. Gusev, K. Bertoldi, and V. Tournat, J. Appl. Phys. **123**, 124901 (2018).
[28]Y. Chen and G. Hu, Phys. Rev. Appl. **12**, 044046 (2019).
[29]M. Zheng, X. Liu, Y. Chen, H. Miao, R. Zhu, and G. Hu, Phys. Rev. Appl. **12**, 014027 (2019).
[30]Y. Chen, X. Liu, and G. Hu, Sci. Rep. **5**, 15745 (2015).
[31]Y. Chen, M. Zheng, X. Liu, Y. Bi, Z. Sun, P. Xiang, J. Yang, and G. Hu, Phys. Rev. B. **95**, 180104 (2017).
[32]C. Il Park, H. M. Seung, J. K. Lee, and Y. Y. Kim, Smart. Mater. Struct. **28**, 75005 (2019).
[33]Y. Liu, Z. Liang, F. Liu, O. Diba, A. Lamb, and J. Li, Phys. Rev. Lett. **119**, 034301 (2017).